FOCUS ISSUE OF SELECTED PAPERS FROM IMLB 2016 WITH INVITED PAPERS CELEBRATING 25 YEARS OF LITHIUM ION BATTERIES

Capacitive vs Faradaic Energy Storage in a Hybrid Cell with $LiFePO_4$/RGO Positive Electrode and Nanocarbon Negative Electrode

Zahilia Cabán-Huertas,[a,*] Deepak P. Dubal,[a] Omar Ayyad,[b] and Pedro Gómez-Romero[a,z]

[a]*Catalan Institute of Nanoscience and Nanotechnology (ICN2), CSIC and The Barcelona Institute of Science and Technology, Campus UAB, Bellaterra, 08193 Barcelona, Spain*
[b]*Faculty of Engineering, Department of Materials Engineering, Al-Quds University, East Jerusalem, Palestine*

We report an advanced device based on a Nitrogen-doped Carbon Nanopipes (N-CNP) negative electrode and a lithium iron phosphate ($LiFePO_4$) positive electrode. We carefully balanced the cell composition (charge balance) and suppressed the initial irreversible capacity of the anode in the round of few cycles. We demonstrated an optimal performance in terms of specific capacity 170 mAh/g of $LiFePO_4$ with energy density of about 203 Wh kg^{-1} and a stable operation for over 100 charge−discharge cycles. The components of this device (combining capacitive and faradaic electrodes) are low cost and easily scalable. This device has a performance comparable to those offered by the present technology of LIBs with the potential for faster charging; hence, we believe that the results disclosed in this work may open up new opportunities for energy storage devices.
 [DOI: 10.1149/2.0211701jes]

Manuscript submitted September 29, 2016; revised manuscript received November 9, 2016. Published November 22, 2016. This was Paper 867 presented at the Chicago, Illinois, Meeting of the IMLB, June 19–24, 2016. *This paper is part of the Focus Issue of Selected Papers from IMLB 2016 with Invited Papers Celebrating 25 Years of Lithium Ion Batteries.*

Lithium ion batteries (LIBs) are presently struggling to meet very demanding standards in terms of cost, charge/discharge rate, power and energy densities, and safety in order to enter new emerging markets such as those of electric vehicles and the storage of renewable electrical energy.[1]

Batteries exhibit relatively high energy densities as a result of faradaic reactions in the bulk of active particles, but are rate-limited. A remarkable example of a well-known material that undergoes a redox process during the battery charge and discharge process is Lithium iron phosphate ($LiFePO_4$). After two decades of the seminal work by Goodenough and col.,[2] $LiFePO_4$ has been established as one of the most widely used positive electrode materials for LIBs thanks to its low cost, abundant raw materials, safety, low toxicity, structural stability and excellent electrochemical properties. The active material can be reversibly charged and discharged with a stable voltage of 3.45 V vs Li^+/Li with a very small change in unit cell parameters during the $LiFePO_4/FePO_4$ phase transition. On the other hand, for the development of high power batteries based on this material, it is essential to understand and overcome the factors limiting lithium transport through the electrode. Indeed, despite its relatively high theoretical specific capacity (170 mAh/g) and long cycling life, the high-rate performance of pure $LiFePO_4$ is restricted by its poor electronic conductivity (10^{-9} S/cm) and slow lithium diffusion.[3] Many different approaches involving surface coating have been tried to improve the capacity and rate performance of $LiFePO_4$ as cathode for LIBs. Increasing the conductivity by coating the $LiFePO_4$ surface with carbon[4,5] or conducting polymers[6,7] have been two of the most popular. In comparison to these carbon materials, graphene can offer an improved interfacial contact because of its superior conductivity, flexible two-dimensional structure, and high surface area.[8] However, due to the thermodynamic instable structure of graphene, it tends to aggregate. Among various graphene derivatives, reduced Graphene Oxide is more polar and hydrophilic than graphene and better conducting that Graphene Oxide and therefore constitutes an optimal choice among graphenes. A critical issue of LIBs technology is the relatively low theoretical specific capacity of conventional graphite anodes, limited to 372 mAh/g.[9]

Electrochemical capacitors[10] can deliver high power at the cost of low energy storage by making use of surface ion adsorption (referred to as double-layer capacitance) and surface redox reactions (referred to as pseudo-capacitance). Lithium rechargeable batteries (energy density 150 W h $Kgcell^{-1}$ and power density 1 KW $kgcell^{-1}$) therefore have higher specific energy but lower specific power than electrochemical capacitors (specific energy 5 W h $Kgcell^{-1}$ and power density 10 KW $Kgcell^{-1}$).[11] Researchers have shown that the gravimetric energy of electrochemical capacitors can be increased by using electrode materials with enhanced gravimetric capacitances (gravimetric charge storage per volt), which can be achieved through the use of carbon subnanometer pores for ion adsorption[12] or by taking advantage of the pseudocapacitance of nanostructured transition metal materials.[13] As an example, our group has developed N-CNPs materials that significantly promote the faradaic contribution as pseudocapacitors, demonstrating high single-electrode capacitance over 332 F/g in 1 M H_2SO_4 aqueous solution.[14] A promising approach is to use the faradaic reactions of surface functional groups on nanostructured carbon electrodes, which can store more energy than the double-layer capacitance on conventional capacitor electrodes and also provide high power capability.[15–17]

All these different mechanisms for charge storage have been traditionally exploited separately.[18] A major challenge in the field of electrical energy storage is to bridge the performance gap between batteries and electrochemical capacitors by developing materials, electrodes and devices that can combine the advantages of each. The hybrid approach allows for a reinforcing combination of properties of dissimilar components in synergic arrangements. From hybrid materials to hybrid devices the approach offers opportunities to tackle much needed improvements in the performance of energy storage devices.[19] Energy and power versatility are crucial for hybrid applications.[20]

Keeping in mind that last thought in mind, Lithium Ion Capacitors (LICs) represent an attempt to bridge the gap between batteries and supercapacitors. Yet, they have been traditionally built with a lithium-insertion (battery-like) anode and a double layer (capacitive) cathode normally made from Activated Carbon (AC). Our initial intention with this work was to explore different possibilities for the design of LICs, namely a combination of a capacitive nanocarbon anode and a well-known faradaic cathode. For this purpose, we chose a novel nanotube-like carbon nanostructure recently reported and one of our optimized $LiFePO_4$/RGO composites as cathode.

*Electrochemical Society Student Member.
[z]E-mail: pedro.gomez@icn2.cat

Experimental

$LiFePO_4$/RGO synthesis.—Typically, 0.0948 g of reduced graphene oxide (RGO) was ultrasonically dispersed in 70 mL of ethylene glycol for 30 min. $LiFePO_4$ was prepared by a reflux method. Stoichiometric amounts (0.12 millimoles) of each precursor; $Li(CH_3COO)\,H_2O$, $Fe(C_2O_4)\cdot 2H_2O$ and H_3PO_4 were dissolved in the 70 ml of RGO-containing ethylene glycol. The reaction mixture was refluxed vigorously for 72 hours at 200°C. The resulting solid was filtered-off, washed several times with deionized water and finally with ethanol. The sample was initially dried at 80°C under vacuum overnight, and then sintered at 700°C for 3 hours under nitrogen atmosphere. The reaction yield was 92% of $LiFePO_4$. See supporting information for RGO synthesis.

N-CNPs synthesis.—5 mM Methyl Orange (MO, sodium 4-[40 (dimethylamino)phenyldiazo] phenylsulfonate ($C_{14}H_{14}N_3NaO_3S$) and 1.5mM$FeCl_3$ (0.243 g) were dissolved in 30 mL deionized (DI) water, resulting in the immediate formation of a flocculent precipitate. In the next step, 0.1 ml (1.5 mM) pyrrole (freshly distilled under vacuum at 130°C) was added to the above solution and the mixture was stirred at room temperature for 24 h. The precipitate formed was filtered-off and repeatedly washed with a mixture of DI water and ethanol (50:50 vol.) to get neutral pH. Finally, the solid was dried overnight under vacuum at 60°C. In order to prepare N-doped carbon nanopipes (N-CNPs), the Polypyrrole-NanoPipes (PPy-NPs) were subjected to pyrolysis at 800 C for 1 h with a heating rate of 5 C/min under N_2 atmosphere.

Materials characterization.—The phase purity and crystal structure of the samples were determined by X-ray diffraction (XRD) using PANalytical X'Pert PRO diffractometer using a Cu Kα radiation source ($\lambda = 1.5418$ Å) in the angular range $10^\circ \leq 2\theta \leq 70^\circ$ at a scan speed of 0.017° per s. The morphology and microstructure of the particles was studied by Scanning Electron Microscopy (SEM, FE Quanta 650F ESEM) and Transmission Electron Microscopy (TEM, Tecnai G2 F20 HRTEM) operated at an acceleration voltage of 200 keV. For TEM studies, samples were dispersed in absolute ethanol, and a drop was then put onto a conventional carbon-coated Cu grid and allowed to evaporate slowly under ambient conditions before being introduced for TEM characterization. Raman scattering (RS) spectra were recorded on a HORIBA Scientific LabRAM HR Raman spectrometer system using Ar laser. The X-ray photoelectron spectroscopy (XPS) analyses were performed with Φ PHYSICAL ELECTRONICS (QUANTUM 2000 SCANNING ESCA MICROPROBE) spectrometer using a focused monochromatized Al K α radiation (1486.6 eV). The residual pressure inside the analysis chamber was 7×10^{-9} Torr. N_2 adsorption/desorption was determined by Brunauer- Emmett-Teller (BET) measurements using Micromeritics instrument (Data Master V4.00Q, Serial#:2000/2400). Elemental organic analysis (C-H-N-S) was carried out by 2400 CHNS/O Series II System (100V).

Electrode preparation.—The cathodes were prepared by pressing a mixture of the active materials with Carbon Super-P (Timcal) and Polyvinylidene fluoride (PVDF) binder in a weight ratio 85/10/5. They were mixed in a mortar for 5 minutes and then dispersed in N-Methyl-2-pyrrolidone and coated onto Al foil.

The anodes were prepared by pressing a mixture of the active material (N-CNPs) with Polyvinylidene fluoride (PVDF) binder in a weight ratio 90/10. They were mixed in a mortar for 5 minutes and then dispersed in N-Methyl-2-pyrrolidone and coated onto Cu foil.

Half cells.—Electrochemical test cells (Swagelok-type) were assembled in an argon-filled glove box with the coated sample electrode as working electrode, lithium metal foil as the counter/reference electrode, and 1 M solution of $LiPF_6$ in a 1:1 vol/vol mixture of ethylene carbonate and diethyl carbonate as the electrolyte. Glass microfiber filter paper was used as separator. $LiFePO_4$/RGO half cell was galvanostatically charged and discharged from 2.5 V to 4.0 V vs Li and the N-CNPs half cells were cycled from 0.3 V to 3 V vs Li at different c-rates.

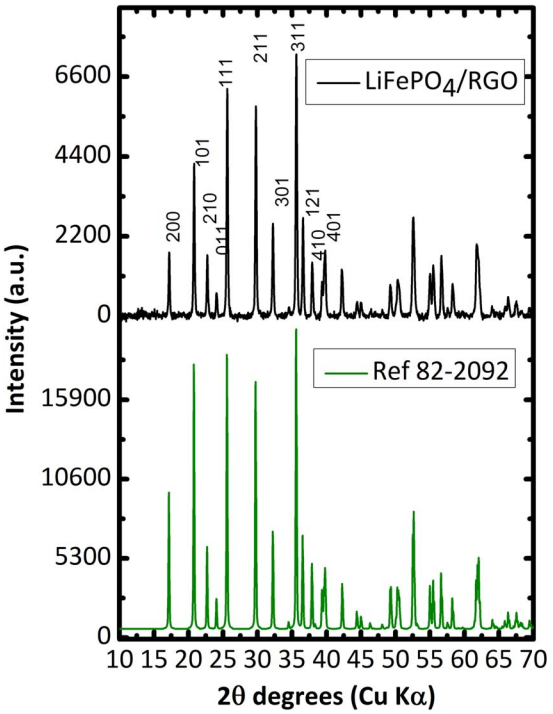

Figure 1. Powder Xray diffraction pattern of $LiFePO_4$/RGO and the reference pattern.

Electrochemical performance of a full cell assembly.—The full $LiFePO_4$/RGO (positive electrode) and NCPs (negative electrode) battery was tested by CV and galvanostatic cycling in Swagelok type cells. After assembling, the full cell was left overnight at open circuit. Then CVs were recorded at 2 mV/s and finally Galvanostatic charge-discharge cycles were carried out at various rates (C/4, C/2, 1C, 2C, 5C, 10C and 1C). The cells were tested using a Biologic VMP3 potentiostat/galvanostat. The full cell was galvanostatically charged and discharged between 0.3 and 4.5 V. Cyclic Voltammetry was performed using the same voltage range. It is important to mention that in the final device, $LiFePO_4$/RGO electrode weight was around 10 mg and the N-CNPs electrodes weight was around 5 mg.

Results

$LiFePO_4$/RGO.—$FePO_4$ nanoparticles were grown on the reduced graphene oxide sheets. With the introduction of Li^+ ions, crystalline $LiFePO_4$ nanosheets nucleated and grew along the ac plane. As shown in Figure 1, XRD patterns of $LiFePO_4$/RGO nanocomposites exhibited a standard orthorhombic $LiFePO_4$ structure (JCPDS No. 83-2092) with space group Pmna and no additional diffraction features. The intense and sharp diffraction peaks indicated a high crystallinity of the materials. In addition, no diffuse carbon diffraction peaks appear at 26° in the $LiFePO_4$/RGO nanocomposites[21] which may be due to its low content and well-exfoliated morphology. The resulting lattice parameters for the $LiFePO_4$/RGO composite ($a = 10.32$ Å, $b = 5.94$ Å, and $c = 4.69$ Å) were nearly identical to those of reference of $LiFePO_4$. The average primary crystallite size, determined from peak width by the Scherrer equation, is about 40 nm.

The presence of carbon in the sample was confirmed by organic elemental analysis. This analysis demonstrates that our sample has 4.6% of carbon. The nature of this carbon material in our sample was

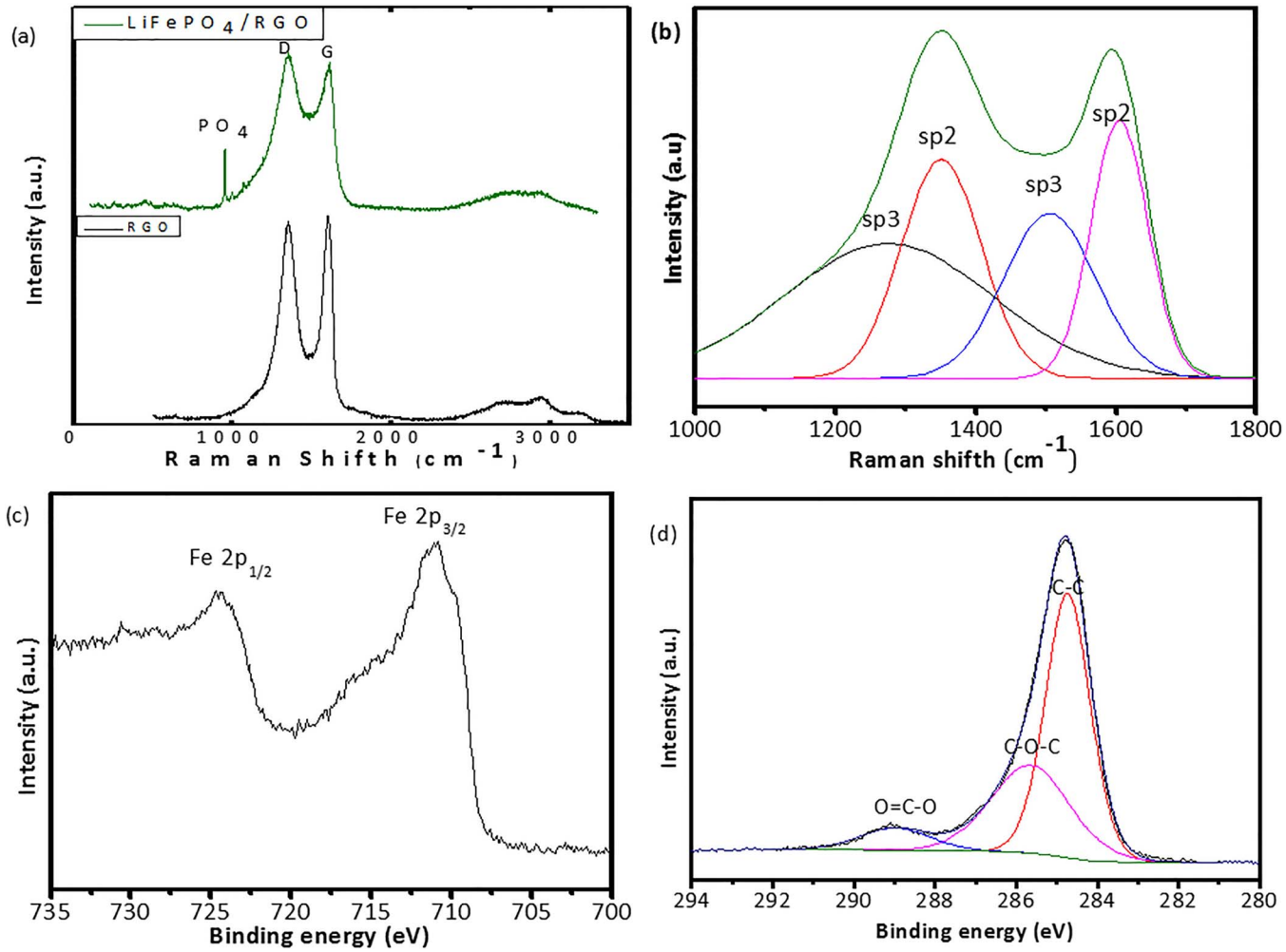

Figure 2. (a) Raman Spectra of RGO and $LiFePO_4$/RGO (b) deconvolution of $LiFePO_4$/RGO Raman spectra (c) XPS narrow spectra of Fe 2p of $LiFePO_4$/RGO (d) C 1s narrow spectra $LiFePO_4$/RGO.

studied by Raman spectroscopy. Figure 2a shows that the $LiFePO_4$/RGO composite shows two characteristic bands at 1353 and 1590 cm^{-1}, assigned to D and G bands of graphene, respectively;[22] these bands are present both in $LiFePO_4$/RGO and RGO. The D band is associated to disorder or defects in the graphene structure, and the E_{2g} vibration mode of the ordered graphitic carbon (G-band). Thus, the intensity ratio of G and D band (I_D/I_G) indicates the degree of disorder. Defects associated to an intense D band can be related to several features: the presence of edges in small crystals, deviations from planarity, the presence of a certain number of carbon atoms with sp^3 hybridization, etc.[23] These spectra show that this sample presents other two bands at 2716.3 and 2953.9 cm^{-1}. The bands correspond to D+G (2953.9 cm^{-1}), a combination scattering peak[24,25] and a second order overtone of a different in-plane vibration (2716.3 cm^{-1}).[25] The D/G intensity ratio of the $LiFePO_4$/RGO composite is 1.1, which is a little bit higher than the RGO I_D/I_G ratio of 1. It is important to point out that the introduction of $LiFePO_4$ nanoparticles distributed on reduced graphene oxide, perturbs the order of the graphene material, and results in less restacking of graphene sheets during reaction. Finally, the peak at 949.6 cm^{-1} corresponds to the PO_4^{-3} anion. The band is very prominent in the spectrum of $LiFePO_4$/RGO. The external modes (lattice vibrations), that occur below 800 cm^{-1} arise primarily due to the vibrational modes related to FeO_6 and LiO_6 octahedra.[26] The intensity ratios of the D and G bands (I_D/I_G) or the total intensity associated to sp^2 to sp^3 carbon vibrations is often used to evaluate the nature of the carbon using the deconvoluted Raman bands.[27] We have fitted the Raman intensity profiles using four Lorentzian lines and have estimated the intensity ratio of $I_{sp2}/I_{sp3} = (I_{1340} + I_{1595})/(I_{1205} + I_{1520}) = 1.5$, Figure 2b. Due to the sp^2/sp^3 ratio the conductivity of the $LiFePO_4$/RGO could be enhanced.

The main focus of our XPS analysis was the Fe 2p core-level. We can observe the core Fe spectra shows the 2 typical bands normally assigned to Fe (II), in $LiFePO_4$ Figure 2c. The main species can be related to Fe (II) at a binding energy of 710 and 723 eV. The C 1s core-level corresponding to $LiFePO_4$/RGO has a well-defined peak at 284.1 eV binding energy, associated to graphene with only a negligible high BE tail due to carbon-oxygen bonds, i.e. C-O-C, C-C and O-C=O, Figure 2d.

Figure 3 shows TEM and STEM images of RGO, and $LiFePO_4$/RGO. The first panel shows RGO sheets partially overlapping with each other. Buckling of the sheets is evident. These images show the flakes and the wrinkles of RGO, particularly in the overlapped regions. Selected Area Electron Diffraction (SAED) pattern from the dotted circle area shows a typical hexagonal symmetry, which is representative of graphene layers. Figure 3b shows the TEM image of $LiFePO_4$/RGO. We can appreciate the curled morphology of RGO and other black regions that could be $LiFePO_4$ nanoparticles that were surrounded by RGO layers. Figure 3c shows a typical high resolution TEM image of the $LiFePO_4$/RGO nanocomposite that demonstrates how $LiFePO_4$ nanoparticles are uniformly distributed onto RGO. This sample is well crystallized single-crystals with similar morphologies according to their Selected Area Electron Diffraction

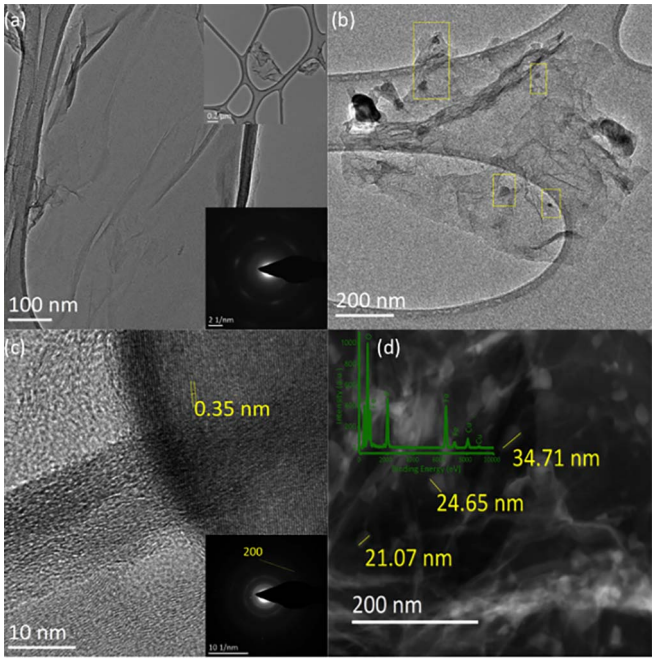

Figure 3. (a) RGO, inset SAED image (b) $LiFePO_4$/RGO TEM images (c) $LiFePO_4$/RGO HRTEM image inset SAED image(d) $LiFePO_4$/RGO STEM image, EDS inset.

(SAED) patterns. The most intense ring in $LiFePO_4$/RGO SAED patterns showed rings which could be indexed as [211] and [220] from the orthorhombic structure, which is consistent with the XRD results and with the d parameter obtained by the HRTEM image. Figure 3d shows the STEM image of the $LiFePO_4$/RGO, this image in addition to the EDS analysis allows to confirm the presence of the $LiFePO_4$ in this composite. Due to space confined effects of RGO, the size of $LiFePO_4$ nanoparticles was also limited to 10 - 35 nm. This particle size could enhance the Li ion diffusion in $LiFePO_4$.[28]

N-CNPs characterization.—In order to acquire more information about the oxidation state of the elements on the surface of the PPy-NPs and N-CNPs, XPS analysis was performed. Figure 4a shows the narrow scan spectra of N1s for PPy-NPs and N-CNPs. Interestingly, PPy-NPs consists of a single peak at 399.7 eV, which is characteristic of neutral nitrogen in PPy rings and is frequently labeled as 'pyrrolic' nitrogen.[29] On the other hand, N-CNPs shows two distinct peaks at 398.2 and 400.9 eV. The former corresponds to the so-called 'pyridinic' nitrogen while peak at 400.9 eV is assigned to 'graphitic' nitrogen. Thus, the peak at 398.2 eV is contributing to the pi-conjugated system and has a lone pair of electrons whereas that at 400.9 eV is observed only when carbon atoms on a graphitic layer are substituted by nitrogen to form the 'graphitic' nitrogen.[30] Ultimately, this XPS analysis shows that nitrogen atoms present in PPy-NPs and N-CNPs are in different oxidation states confirming the formation of N-CNPs. The graphitic N doped inside the aromatic ring (quaternary N) introduces a positive charge and electron acceptor properties, consequently enhancing the conductivity of this carbon material.

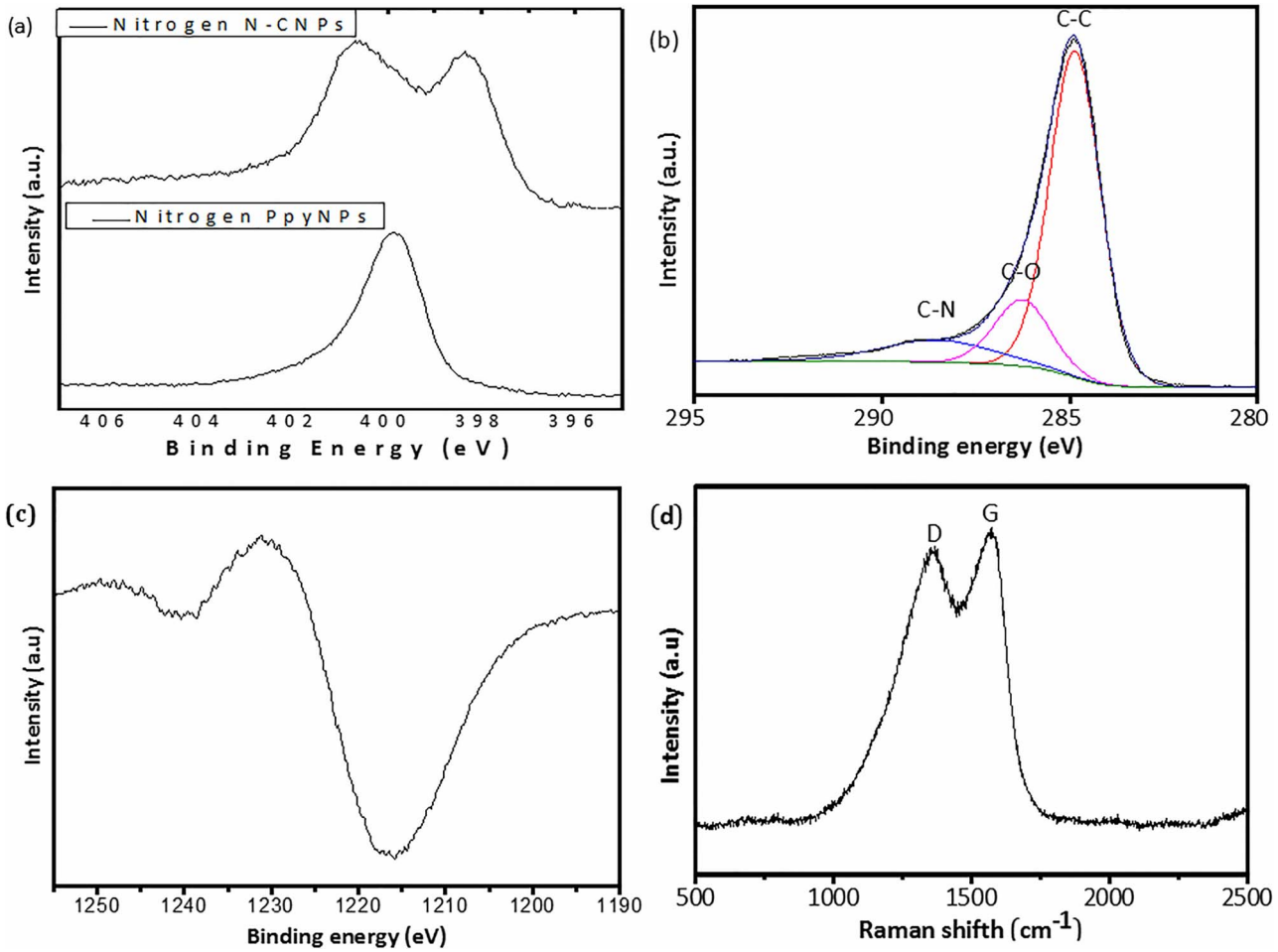

Figure 4. (a) Nitrogen XPS narrow scan of PPy-NPs and N-CNPS (b) Carbon narrow spectra of N-CNPS (c) first derivate of carbon auger peak of N-CNPS (d) Raman spectra of N-CNPs.

The narrow scan spectrum of C1s for N-CNPs (Figure 4b), shows a broad feature which can be deconvoluted into three peaks centered at binding energies of 284.6, 285.5 and 287.7 eV. The peak at 284.6 eV confirms the presence of graphitic carbon, corresponding to the energy of the sp^2 C=C bond in the C1s spectrum of pyrolytic graphite. The weaker features at higher binding energies correspond to C-O (285.5 eV) and C-N (287.7 eV) species in N-CNPs, respectively.[31] We also calculated de D parameter of the N-CNPs sample. The D parameter is a finger print of carbon, giving the ability to distinguish between sp^2 and sp^3 carbon. This parameter can be obtained by the analysis of the auger peak of carbon and their respective derivate. This sample shows a D parameter of 16 eV, which means this sample has an sp2 component of ca 33%,[32] Figure 4c.

Besides XPS, Raman Spectra gives more information about the composition of the samples, Figure 4d. N-CNPs exhibits the two bands characteristic of graphitic carbons at 1355 (D band) and 1571 cm^{-1} (G band). The D band originates from disorder-induced amorphous carbon due to the finite particle size effect, lattice distortion, and/or the presence of structural defects. On the other hand, the G band is assigned to graphite since the shift of highly oriented pyrolytic graphite is found at 1572 cm^{-1}. The relative intensity of G band with respect to D band (I_G/I_D) indicates the degree of order of N-CNPs, which depends on the crystal planar domain size of graphite. It has been estimated that I_G/I_D for N-CNPs is found to be 0.96, suggesting a low level of defects for CNPs.[33]

In order to get more insights about the microstructure, size and shape of the samples, SEM and STEM analyses were carried out and are shown in Figure 5a. The N-CNPs exhibit inner diameters in the range of 50–75 nm. The PPy-Nps exhibits outer and inner diameters about 170–190 nm and inner diameter between 85–105 nm. It should be remarked that although the diameter of the nanopipes decreases with thermal treatment converting PPy nanopipes into N-CNPs, this thermal treatment did not change the morphology of the pipes Figure 5b.

Surface area and pore-size distribution analysis of N-CNPs were carried out using N_2 adsorption and desorption experiments. As seen from Figure 6a, the profile of the hysteresis loop indicates adsorption-desorption characteristics of a porous materials. The BET specific surface area of N-CNPs materials obtained was 58.9 $m^2\ g^{-1}$. The BJH pore size distribution of N-CNPs samples were calculated using

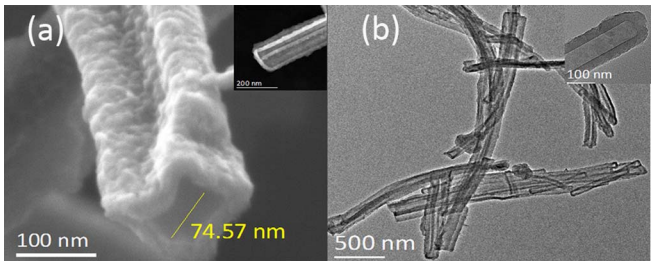

Figure 5. (a) SEM and STEM (b) TEM images of N-CNPs inset ppy-NPs.

the desorption curve. The curve in Figure 6b reveals the presence of hierarchical porosity: <2 nm micropores, 4 nm mesopores and 20–100 nm macro/mesopores, which is an optimal configuration to provide a large electric-double-layer capacitance.

Electrochemistry.—Figure 7a includes cyclic voltammograms of the N-CNPs and $LiFePO_4$/RGO electrodes between 0 - 3 V vs Li/Li^+ and 2.5 – 4 V vs Li^+ respectively at 1 mV/s. The most obvious difference between both electrodes is the faradaic behavior of the later, with well-defined redox waves at characteristic potentials compared to the essentially capacitive behavior of N-CNPs. It should be noted though that the nanopipes electrode shows broad waves indicative of a faradaic behavior possibly associated to redox processes from N-doping. In any event, both electrodes are complementary in their charge capacity and they work within a large stability window of the $LiPF_6$/EC-DMC electrolyte Based on these CVs we could conceive a cell combining N-CNPs negative and $LiFePO_4$/RGO positive electrodes cycling between ca. 0.5 V and 4.5 V vs Li/Li^+. Before setting up such a cell we carried out charge-discharge cycles for each of the two electrodes vs Li. The results of N-CNPs Half-cells is shown in Figure 7b.

It is remarkable that the N-CNPs electrode leads to capacity values of up to 351 mAh/g, comparable with the capacity of graphite (372 mAh/g), when cycled between 3.0 and 0.3 V vs Li/Li^+ (well above the possible deposition of metallic Li). Despite the essentially linear profile of the charge and discharge curves (characteristic of capacitive storage) the large capacity points to certain degree of Li^+

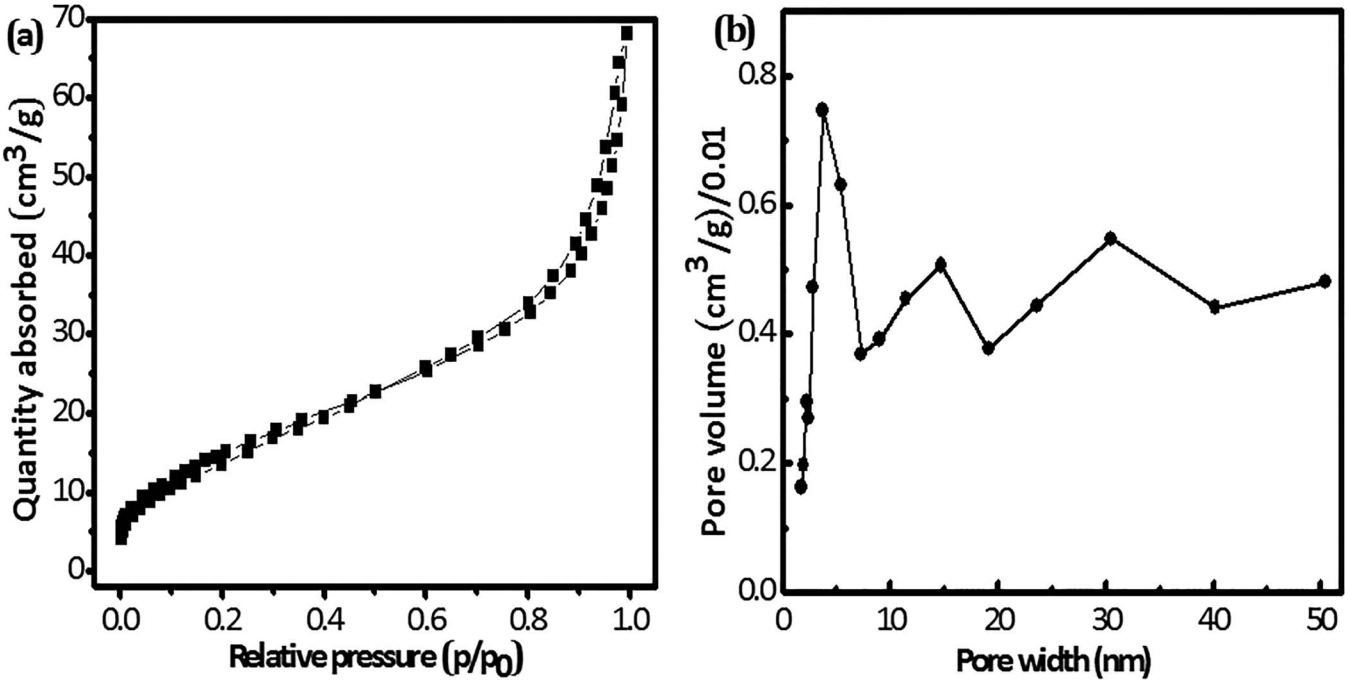

Figure 6. (a) Adbsortion and deabsortion of N_2 (BET) (b) Pore size (BJH) of N-CNPs.

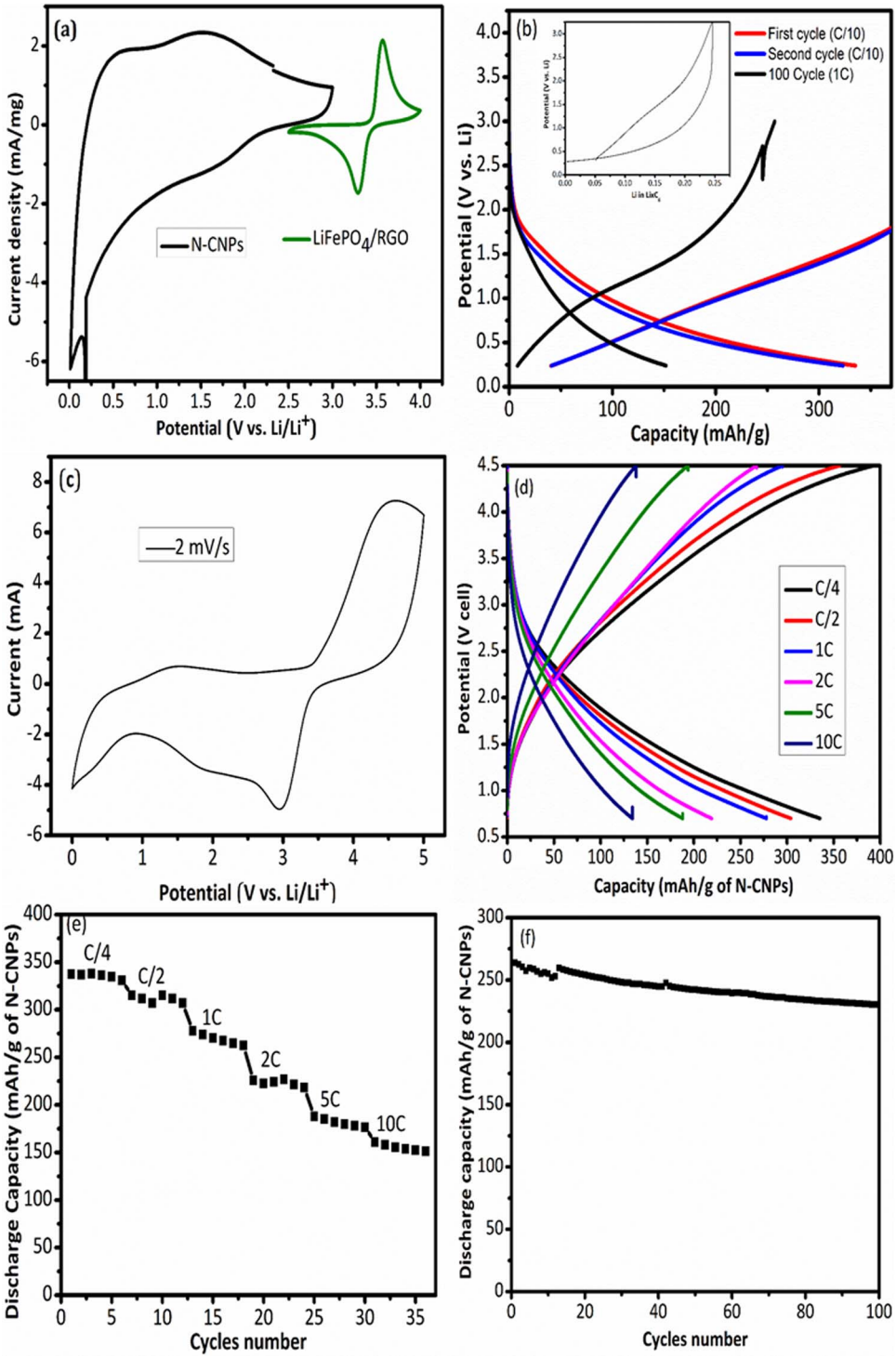

Figure 7. (a) CV of N-CNPs and $LiFePO_4$/RGO at 1 mV/s (b) voltage profile of N-CNPs (different cycles) and typical potential profile of the Li composition (c) CV of the cell at 2 mV-s (d) potential vs capacity profile of the cell (e) rate capability of the cell at different C-Rates (f) stability test at 1C for 100 cycles.

intercalation-deintercalation is possibly associated to surface nitrogen groups in the negative electrode materials The N-CNPs sample on the other hand does not show a stable plateau. We have carried out that simple calculation for our preliminary chronopotentiometric experiments (N-CNPipes vs Li metal) and got 0.25 atoms of Li per C atom incorcoprated to N-CNPipes ($CLi_{0.25}$). Remarkably, a greater Li loading than for graphite in a nanocarbons electrode faster than batteries with graphite anodes.

$LiFePO_4$/RGO yields capacity values of 167 mAh/g (between 2.5 and 4.0 V vs Li/Li^+), very close to the theoretical value of 170 mAh/g for conventional C-coated $LiFePO_4$ electrodes, with a very nice plateau at 3.45 V vs Li/Li^+ at C rate of C/10. We should mention that we did the calculations to obtain the real $LiFePO_4$ mass on the electrode and this was the mass used to obtain the capacity of the $LiFePO_4$/RGO electrode. More details like rate capability are discussed in the supplementary information.

The CV of the full device ($LiFePO_4$/RGO positive and N-CNPs negative electrodes) shows a complex shape resulting from the combination of voltage-independent capacitive behavior and voltage-specific faradaic processes, the latter corresponding to $LiFePO_4$ reduction (3.0 V) and oxidation (4.5 V) processes, Figure 7c.

In designing the battery, it is very important to reach an optimal balance of cathode and anode electrodes both in terms of weight and electrochemical activities, as mentioned in the Experimental section. The device is characterized by a slight excess of anode capacity, achieved by balancing the mass (1:2 mass ratio) of N-CNPs respect to $LiFePO_4$/RGO. Figure 7d shows a charge-discharge profile demonstrating a constant polarization, as it could be expected. The battery operates around 2.3 V, with a reversible capacity of 342 mAh/g. Figure 7e shows the rate capability of the full device. It is remarkable that we can cycle this device at a C/4 rate to obtain the maximum theoretical capacity in terms of $LiFePO_4$, whereas in the case of the half-cell of $LiFePO_4$ vs Li metal the maximum capacity was obtained at C/10. This is an indication of a faster charge process for our full cell and the consequent possibility of improvement. Finally, the cycling performance of the full cell at 1C rate in Figure 7f shows the stability of the device, over 100 cycles. However, there is a small decay in the capacity of the device. At the end of the 100 cycles the capacity obtained was the 84% of the initial capacity at 1C.

Conclusions

We have shown for the first time the possible application of novel N-doped Carbon Nanopipes (N-CNPs) as negative electrodes in energy storage devices. In principle, this carbon material was spotted as a possible capacitive (Double-Layer) electrode which could be used to set up a hybrid device. Our work has shown that actually these wide N-CNPs (ca. 75 nm inner diameter) can sustain lithium intercalation and work as negative electrodes in a full battery cell confronted with $LiFePO_4$. We carefully balanced the cell composition (charge balance) and suppressed the initial irreversible capacity of the anode in the round of few cycles. We demonstrated an optimal performance in terms of specific capacity (170 mAh/g of $LiFePO_4$) with energy density of about 203 Wh kg^{-1} and a stable operation for over 100 charge−discharge cycles.

Acknowledgments

The research leading to these results received funding from the European Commission Seventh Framework program (FP7/2007–2013) under grant Agreement. 266090 (SOMABAT). NESTOR Nanomaterials for Energy STORage. Partial funding from AGAUR Generalitat de Catalunya 2014_SGR_1505 and MINECOProyecto MAT2015-68394-R (NaCarFLOW) is also acknowledged.

References

1. M. Armand and J. M. Tarascon, *Nature*, **451**, 652 (2008).
2. A. K. Padhi, K. S. Nanjundaswamy, and J. B. Goodenough, *J. Electrochem. Soc.*, **144**, 1188 (1997).
3. Y.-N. Xu, S.-Y. Chung, J. T. Bloking, Y.-M. Chiang, and W. Y. Ching, *Electrochem. Solid-State Lett.*, **7**, A131 (2004).
4. N. Ravet, Y. Chouinard, J. F. Magnan, S. Besner, M. Gauthier, and M. Armand, *J. Power Sources*, **97–98**, 503 (2001).
5. Z. Cabán-Huertas, O. Ayyad, D. P. Dubal, and P. Gómez-Romero, *Scientific Reports*, **6**, 27024 (2016).
6. A. Fedorková, A. Nacher-Alejos, P. Gómez-Romero, R. Oriňáková, and D. Kaniansky, *Electrochim. Acta*, **55**, 943 (2010).
7. A. V. Murugan, T. Muraliganth, and A. Manthiram, *ECS Transactions*, **16**, 49 (2009).
8. Y. Zhu, S. Murali, W. Cai, X. Li, J. W. Suk, J. R. Potts, and R. S. Ruoff, *Adv. Mater.*, **22**, 3906 (2010).
9. B. Scrosati and J. Garche, *J. Power Sources*, **195**, 2419 (2010).
10. G. G. Amatucci, F. Badway, A. Du Pasquier, and T. Zheng, *J. Electrochem. Soc.*, **148**, A930 (2001).
11. P. Simon and Y. Gogotsi, *Nat Mater*, **7**, 845 (2008).
12. J. Chmiola, G. Yushin, Y. Gogotsi, C. Portet, P. Simon, and P. L. Taberna, *Science*, **313**, 1760 (2006).
13. A. David, G. Pascal, R. Vanesa, G.-R. Pedro, W. Jan, I. Boyan, J. S. S. Thomas, S. Saïd, and B. Gérard, *Advances in Natural Sciences: Nanoscience and Nanotechnology*, **6**, 015004 (2015).
14. D. P. Dubal, N. R. Chodankar, Z. Caban-Huertas, F. Wolfart, M. Vidotti, R. Holze, C. D. Lokhande, and P. Gomez-Romero, *J. Power Sources*, **308**, 158 (2016).
15. F. Wolfart, D. P. Dubal, M. Vidotti, and P. Gomez-Romero, *RSC Advances*, **6**, 15062 (2016).
16. J. Suarez-Guevara, V. Ruiz, and P. Gomez-Romero, *PCCP*, **16**, 20411 (2014).
17. J. Suarez-Guevara, V. Ruiz, and P. Gomez-Romero, *Journal of Materials Chemistry A*, **2**, 1014 (2014).
18. H. D. Abruña, Y. Kiya, and J. C. Henderson, *Physics Today* **61**, 43 (2008).
19. D. P. Dubal, O. Ayyad, V. Ruiz, and P. Gomez-Romero, *Chem. Soc. Rev.*, **44**, 1777 (2015).
20. J. R. Miller and P. Simon, *Science*, **321**, 651 (2008).
21. B. Wang, D. Wang, Q. Wang, T. Liu, C. Guo, and X. Zhao, *Journal of Materials Chemistry A*, **1**, 135 (2013).
22. J. Mun, H.-W. Ha, and W. Choi, *J. Power Sources*, **251**, 386 (2014).
23. C. R. Minitha and R. T. Rajendrakumar, *Advanced Materials Research*, **678**, 56 (2013).
24. R. Saito, A. Jorio, A. G. Souza Filho, G. Dresselhaus, M. S. Dresselhaus, and M. A. Pimenta, *Phys. Rev. Lett.*, **88**, 027401 (2001).
25. R. Saito, M. Hofmann, G. Dresselhaus, A. Jorio, and M. S. Dresselhaus, *Adv. Phys.*, **60**, 413 (2011).
26. C. M. Burba and R. Frech, *J. Electrochem. Soc.*, **151**, A1032 (2004).
27. M. M. Doeff, Y. Hu, F. McLarnon, and R. Kostecki, *Electrochem. Solid-State Lett.*, **6**, A207 (2003).
28. R. Malik, D. Burch, M. Bazant, and G. Ceder, *Nano Lett.*, **10**, 4123 (2010).
29. N. Su, H. B. Li, S. J. Yuan, S. P. Yi, and E. Q. Yin, *eXpress Polymer Letters*, **6**, 697 (2012).
30. Z.-H. Sheng, L. Shao, J.-J. Chen, W.-J. Bao, F.-B. Wang, and X.-H. Xia, *ACS Nano*, **5**, 4350 (2011).
31. H. Ago, T. Kugler, F. Cacialli, W. R. Salaneck, M. S. P. Shaffer, A. H. Windle, and R. H. Friend, *The Journal of Physical Chemistry B*, **103**, 8116 (1999).
32. A. Mezzi and S. Kaciulis, *Surf. Interface Anal.*, **42**, 1082 (2010).
33. A. C. Ferrari and J. Robertson, *Physical Review B*, **64**, 075414 (2001).